**Authors**

Jennifer L Ellis, Kevin M Dorney, Charles G Durfee, Carlos Hernández-García, Franklin Dollar, Christopher A Mancuso, Tingting Fan, Dmitriy Zusin, Christian Gentry, Patrik Grychtol, Henry C Kapteyn, Margaret M Murnane, and Daniel D Hickstein

**Research Article** Vol. 25, No. 9 | 1 May 2017 | OPTICS EXPRESS 10126

Optics EXPRESS

# Phase matching of noncollinear sum and difference frequency high harmonic generation above and below the critical ionization level

JENNIFER L. ELLIS,[1,*] KEVIN M. DORNEY,[1] CHARLES G. DURFEE,[1,2] CARLOS HERNÁNDEZ-GARCÍA,[3] FRANKLIN DOLLAR,[1] CHRISTOPHER A. MANCUSO,[1] TINGTING FAN,[1] DMITRIY ZUSIN,[1] CHRISTIAN GENTRY,[1] PATRIK GRYCHTOL,[1] HENRY C. KAPTEYN,[1] MARGARET M. MURNANE,[1] AND DANIEL D. HICKSTEIN[1]

[1] *JILA – NIST and Department of Physics, University of Colorado, Boulder, CO, USA*
[2] *Department of Physics, Colorado School of Mines, Golden, CO, USA*
[3] *Grupo de Investigación en Aplicaciones del Láser y Fotónica, Departamento de Física Aplicada, University of Salamanca, Salamanca, Spain*
[*] *jennifer.ellis@colorado.edu*

**Abstract:** We investigate the macroscopic physics of noncollinear high harmonic generation (HHG) at high pressures. We make the first experimental demonstration of phase matching of noncollinear high-order-difference-frequency generation at ionization fractions above the critical ionization level, which normally sets an upper limit on the achievable cutoff photon energies. Additionally, we show that noncollinear high-order-sum-frequency generation requires much higher pressures for phase matching than single-beam HHG does, which mitigates the short interaction region in this geometry. We also dramatically increase the experimentally realized cutoff energy of noncollinear circularly polarized HHG, reaching photon energies of 90 eV. Finally, we achieve complete angular separation of high harmonic orders without the use of a spectrometer.

**OCIS codes:** (020.2649) Strong field laser physics; (020.4180) Multiphoton processes; (190.2620) Harmonic generation and mixing.

## References and links

1. A. McPherson, G. Gibson, H. Jara, U. Johann, T. S. Luk, I. A. McIntyre, K. Boyer, and C. K. Rhodes, "Studies of multiphoton production of vacuum-ultraviolet radiation in the rare gases," J. Opt. Soc. Am. B **4**(4), 595–601 (1987).
2. M. Ferray, A. L'Huillier, X. F. Li, L. A. Lompre, G. Mainfray, and C. Manus, "Multiple-harmonic conversion of 1064 nm radiation in rare gases," J. Phys. B **21**(3), L31–L35 (1988).
3. A. Rundquist, C. G. Durfee 3rd, Z. Chang, C. Herne, S. Backus, M. M. Murnane, and H. C. Kapteyn, "Phase-matched generation of coherent soft X-rays," Science **280**(5368), 1412–1415 (1998).
4. R. A. Bartels, A. Paul, H. Green, H. C. Kapteyn, M. M. Murnane, S. Backus, I. P. Christov, Y. Liu, D. Attwood, and C. Jacobsen, "Generation of spatially coherent light at extreme ultraviolet wavelengths," Science **297**(5580), 376–378 (2002).
5. F. Silva, S. M. Teichmann, S. L. Cousin, M. Hemmer, and J. Biegert, "Spatiotemporal isolation of attosecond soft X-ray pulses in the water window," Nat. Commun. **6**, 6611 (2015).
6. E. R. Shanblatt, C. L. Porter, D. F. Gardner, G. F. Mancini, R. M. Karl, Jr., M. D. Tanksalvala, C. S. Bevis, V. H. Vartanian, H. C. Kapteyn, D. E. Adams, and M. M. Murnane, "Quantitative chemically-specific coherent diffractive imaging of reactions at buried interfaces with few-nanometer precision," Nano Lett. **16**(9), 5444–5450 (2016).
7. K. M. Hoogeboom-Pot, J. N. Hernandez-Charpak, X. Gu, T. D. Frazer, E. H. Anderson, W. Chao, R. W. Falcone, R. Yang, M. M. Murnane, H. C. Kapteyn, and D. Nardi, "A new regime of nanoscale thermal transport: Collective diffusion increases dissipation efficiency," Proc. Natl. Acad. Sci. U.S.A. **112**(16), 4846–4851 (2015).
8. J. L. Ellis, D. D. Hickstein, W. Xiong, F. Dollar, B. B. Palm, K. E. Keister, K. M. Dorney, C. Ding, T. Fan, M. B. Wilker, K. J. Schnitzenbaumer, G. Dukovic, J. L. Jimenez, H. C. Kapteyn, and M. M. Murnane, "Materials properties and solvated electron dynamics of isolated nanoparticles and nanodroplets probed with ultrafast

#280221 https://doi.org/10.1364/OE.25.010126
Journal © 2017 Received 7 Nov 2016; accepted 6 Apr 2017; published 25 Apr 2017

extreme ultraviolet beams," J. Phys. Chem. Lett. **7**(4), 609–615 (2016).

9. Z. Tao, C. Chen, T. Szilvási, M. Keller, M. Mavrikakis, H. Kapteyn, and M. Murnane, "Direct time-domain observation of attosecond final-state lifetimes in photoemission from solids," Science **353**(6294), 62–67 (2016).
10. A. L. Cavalieri, N. Müller, T. Uphues, V. S. Yakovlev, A. Baltuška, B. Horvath, B. Schmidt, L. Blümel, R. Holzwarth, S. Hendel, M. Drescher, U. Kleineberg, P. M. Echenique, R. Kienberger, F. Krausz, and U. Heinzmann, "Attosecond spectroscopy in condensed matter," Nature **449**(7165), 1029–1032 (2007).
11. S. Neppl, R. Ernstorfer, A. L. Cavalieri, C. Lemell, G. Wachter, E. Magerl, E. M. Bothschafter, M. Jobst, M. Hofstetter, U. Kleineberg, J. V. Barth, D. Menzel, J. Burgdörfer, P. Feulner, F. Krausz, and R. Kienberger, "Direct observation of electron propagation and dielectric screening on the atomic length scale," Nature **517**(7534), 342–346 (2015).
12. M. Eckstein, C.-H. Yang, F. Frassetto, L. Poletto, G. Sansone, M. J. J. Vrakking, and O. Kornilov, "Direct imaging of transient Fano resonances in N2 using time-, energy-, and angular-resolved photoelectron spectroscopy," Phys. Rev. Lett. **116**(16), 163003 (2016).
13. S. Mathias, C. La-o-vorakiat, J. M. Shaw, E. Turgut, P. Grychtol, R. Adam, D. Rudolf, H. T. Nembach, T. J. Silva, M. Aeschlimann, C. M. Schneider, H. C. Kapteyn, and M. M. Murnane, "Ultrafast element-specific magnetization dynamics of complex magnetic materials on a table-top," J. Electron Spectrosc. Relat. Phenom. **189**, 164–170 (2013).
14. Y. Pertot, C. Schmidt, M. Matthews, A. Chauvet, M. Huppert, V. Svoboda, A. von Conta, A. Tehlar, D. Baykusheva, J.-P. Wolf, and H. J. Wörner, "Time-resolved x-ray absorption spectroscopy with a water window high-harmonic source," Science **355**(6322), 264–267 (2017).
15. L. R. Baker, C.-M. Jiang, S. T. Kelly, J. M. Lucas, J. Vura-Weis, M. K. Gilles, A. P. Alivisatos, and S. R. Leone, "Charge carrier dynamics of photoexcited Co3O4 in methanol: extending high harmonic transient absorption spectroscopy to liquid environments," Nano Lett. **14**(10), 5883–5890 (2014).
16. K. Zhang, M.-F. Lin, E. S. Ryland, M. A. Verkamp, K. Benke, F. M. F. de Groot, G. S. Girolami, and J. Vura-Weis, "Shrinking the synchrotron: Tabletop extreme ultraviolet absorption of transition-metal complexes," J. Phys. Chem. Lett. **7**(17), 3383–3387 (2016).
17. M. Holler, F. Schapper, L. Gallmann, and U. Keller, "Attosecond electron wave-packet interference observed by transient absorption," Phys. Rev. Lett. **106**(12), 123601 (2011).
18. S. Long, W. Becker, and J. K. McIver, "Model calculations of polarization-dependent two-color high-harmonic generation," Phys. Rev. A **52**(3), 2262–2278 (1995).
19. H. Eichmann, A. Egbert, S. Nolte, C. Momma, B. Wellegehausen, W. Becker, S. Long, and J. K. McIver, "Polarization-dependent high-order two-color mixing," Phys. Rev. A **51**(5), R3414–R3417 (1995).
20. X.-M. Tong and S.-I. Chu, "Generation of circularly polarized multiple high-order harmonic emission from two-color crossed laser beams," Phys. Rev. A **58**(4), R2656–R2659 (1998).
21. D. B. Milošević and W. Becker, "Attosecond pulse trains with unusual nonlinear polarization," Phys. Rev. A **62**(1), 011403 (2000).
22. A. Fleischer, O. Kfir, T. Diskin, P. Sidorenko, and O. Cohen, "Spin angular momentum and tunable polarization in high-harmonic generation," Nat. Photonics **8**(7), 543–549 (2014).
23. E. Pisanty, S. Sukiasyan, and M. Ivanov, "Spin conservation in high-order-harmonic generation using bicircular fields," Phys. Rev. A **90**(4), 043829 (2014).
24. O. Kfir, P. Grychtol, E. Turgut, R. Knut, D. Zusin, D. Popmintchev, T. Popmintchev, H. Nembach, J. M. Shaw, A. Fleischer, H. Kapteyn, M. Murnane, and O. Cohen, "Generation of bright phase-matched circularly-polarized extreme ultraviolet high harmonics," Nat. Photonics **9**(2), 99–105 (2014).
25. A. Ferré, C. Handschin, M. Dumergue, F. Burgy, A. Comby, D. Descamps, B. Fabre, G. A. Garcia, R. Géneaux, L. Merceron, E. Mével, L. Nahon, S. Petit, B. Pons, D. Staedter, S. Weber, T. Ruchon, V. Blanchet, and Y. Mairesse, "A table-top ultrashort light source in the extreme ultraviolet for circular dichroism experiments," Nat. Photonics **9**(2), 93–98 (2014).
26. T. Fan, P. Grychtol, R. Knut, C. Hernández-García, D. D. Hickstein, D. Zusin, C. Gentry, F. J. Dollar, C. A. Mancuso, C. W. Hogle, O. Kfir, D. Legut, K. Carva, J. L. Ellis, K. M. Dorney, C. Chen, O. G. Shpyrko, E. E. Fullerton, O. Cohen, P. M. Oppeneer, D. B. Milošević, A. Becker, A. A. Jaroń-Becker, T. Popmintchev, M. M. Murnane, and H. C. Kapteyn, "Bright circularly polarized soft X-ray high harmonics for X-ray magnetic circular dichroism," Proc. Natl. Acad. Sci. U.S.A. **112**(46), 14206–14211 (2015).
27. G. Lambert, B. Vodungbo, J. Gautier, B. Mahieu, V. Malka, S. Sebban, P. Zeitoun, J. Luning, J. Perron, A. Andreev, S. Stremoukhov, F. Ardana-Lamas, A. Dax, C. P. Hauri, A. Sardinha, and M. Fajardo, "Towards enabling femtosecond helicity-dependent spectroscopy with high-harmonic sources," Nat. Commun. **6**, 6167 (2015).
28. D. D. Hickstein, F. J. Dollar, P. Grychtol, J. L. Ellis, R. Knut, C. Hernández-García, D. Zusin, C. Gentry, J. M. Shaw, T. Fan, K. M. Dorney, A. Becker, A. Jaroń-Becker, H. C. Kapteyn, M. M. Murnane, and C. G. Durfee, "Non-collinear generation of angularly isolated circularly polarized high harmonics," Nat. Photonics **9**(11), 743–750 (2015).
29. C. M. Heyl, S. N. Bengtsson, S. Carlström, J. Mauritsson, C. L. Arnold, and A. L'Huillier, "Noncollinear optical gating," New J. Phys. **16**(5), 052001 (2014).
30. M. Louisy, C. L. Arnold, M. Miranda, E. W. Larsen, S. N. Bengtsson, D. Kroon, M. Kotur, D. Guénot, L. Rading, P. Rudawski, F. Brizuela, F. Campi, B. Kim, A. Jarnac, A. Houard, J. Mauritsson, P. Johnsson, A. L'Huillier, and C. M. Heyl, "Gating attosecond pulses in a noncollinear geometry," Optica **2**(6), 563–566 (2015).

31. C. Hernández-García, C. G. Durfee, D. D. Hickstein, T. Popmintchev, A. Meier, M. M. Murnane, H. C. Kapteyn, I. J. Sola, A. Jaron-Becker, and A. Becker, "Schemes for generation of isolated attosecond pulses of pure circular polarization," Phys. Rev. A **93**(4), 043855 (2016).
32. P.-C. Huang, C.-H. Lu, C. Hernandez-Garcia, R.-T. Huang, P.-S. Wu, D. D. Hickstein, D. Thrasher, J. L. Ellis, A. H. Kung, S.-D. Yang, A. Jaron-Becker, A. Becker, H. C. Kapteyn, M. M. Murnane, C. G. Durfee, and M.-C. Chen, "Isolated, circularly polarized, attosecond pulse generation," in *International Conference on Ultrafast Phenomena* (OSA, 2016), p. UTh5A.4.
33. A. V. Birulin, V. T. Platonenko, and V. V. Strelkov, "High-order harmonic generation in colliding beams," Quantum Electron. **26**(5), 377–378 (1996).
34. J. Peatross, J. L. Chaloupka, and D. D. Meyerhofer, "High-order harmonic generation with an annular laser beam," Opt. Lett. **19**(13), 942–944 (1994).
35. S. V. Fomichev, P. Breger, B. Carré, P. Agostini, and D. F. Zaretsky, "Non-collinear high-harmonic generation," Laser Phys. **12**, 383–388 (2002).
36. M. Negro, M. Devetta, D. Faccialá, A. G. Ciriolo, F. Calegari, F. Frassetto, L. Poletto, V. Tosa, C. Vozzi, and S. Stagira, "Non-collinear high-order harmonic generation by three interfering laser beams," Opt. Express **22**(24), 29778–29786 (2014).
37. J. B. Bertrand, H. J. Wörner, H.-C. Bandulet, É. Bisson, M. Spanner, J.-C. Kieffer, D. M. Villeneuve, and P. B. Corkum, "Ultrahigh-order wave mixing in noncollinear high harmonic generation," Phys. Rev. Lett. **106**(2), 023001 (2011).
38. A. Ozawa, A. Vernaleken, W. Schneider, I. Gotlibovych, T. Udem, and T. W. Hänsch, "Non-collinear high harmonic generation: a promising outcoupling method for cavity-assisted XUV generation," Opt. Express **16**(9), 6233–6239 (2008).
39. J. Wu and H. Zeng, "Cavity-enhanced noncollinear high-harmonic generation for extreme ultraviolet frequency combs," Opt. Lett. **32**(22), 3315–3317 (2007).
40. K. D. Moll, R. J. Jones, and J. Ye, "Output coupling methods for cavity-based high-harmonic generation," Opt. Express **14**(18), 8189–8197 (2006).
41. R. Rajeev, J. Hellwagner, A. Schumacher, I. Jordan, M. Huppert, A. Tehlar, B. R. Niraghatam, D. Baykusheva, N. Lin, A. von Conta, and H. J. Wörner, "In situ frequency gating and beam splitting of vacuum- and extreme-ultraviolet pulses," Light Sci. Appl. **5**(11), e16170 (2016).
42. K. T. Kim, C. Zhang, A. D. Shiner, S. E. Kirkwood, E. Frumker, G. Gariepy, A. Naumov, D. M. Villeneuve, and P. B. Corkum, "Manipulation of quantum paths for space–time characterization of attosecond pulses," Nat. Phys. **9**(3), 159–163 (2013).
43. C. M. Heyl, P. Rudawski, F. Brizuela, S. N. Bengtsson, J. Mauritsson, and A. L'Huillier, "Macroscopic effects in noncollinear high-order harmonic generation," Phys. Rev. Lett. **112**(14), 143902 (2014).
44. C. G. Durfee, A. R. Rundquist, S. Backus, C. Herne, M. M. Murnane, and H. C. Kapteyn, "Phase matching of high-order harmonics in hollow waveguides," Phys. Rev. Lett. **83**(11), 2187–2190 (1999).
45. E. Constant, D. Garzella, P. Breger, E. Mével, C. Dorrer, C. Le Blanc, F. Salin, and P. Agostini, "Optimizing high harmonic generation in absorbing gases: Model and experiment," Phys. Rev. Lett. **82**(8), 1668–1671 (1999).
46. M. Schnürer, Z. Cheng, M. Hentschel, G. Tempea, P. Kálmán, T. Brabec, and F. Krausz, "Absorption-limited generation of coherent ultrashort soft-x-ray pulses," Phys. Rev. Lett. **83**(4), 722–725 (1999).
47. E. J. Takahashi, T. Kanai, K. L. Ishikawa, Y. Nabekawa, and K. Midorikawa, "Coherent water window x ray by phase-matched high-order harmonic generation in neutral media," Phys. Rev. Lett. **101**(25), 253901 (2008).
48. A. Averchi, D. Faccio, R. Berlasso, M. Kolesik, J. V. Moloney, A. Couairon, and P. Di Trapani, "Phase matching with pulsed Bessel beams for high-order harmonic generation," Phys. Rev. A **77**(2), 021802 (2008).
49. J. L. Silva, H. M. Crespo, and R. Weigand, "Generation of high-energy vacuum UV femtosecond pulses by multiple-beam cascaded four-wave mixing in a transparent solid," Appl. Opt. **50**(14), 1968–1973 (2011).
50. V. Vaičaitis, V. Jarutis, K. Steponkevičius, and A. Stabinis, "Noncollinear six-wave mixing of femtosecond laser pulses in air," Phys. Rev. A **87**(6), 063825 (2013).
51. P. L. Shkolnikov, A. E. Kaplan, and A. Lago, "Phase matching for large-scale frequency upconversion in plasma," Opt. Lett. **18**(20), 1700–1702 (1993).
52. O. Cohen, T. Popmintchev, D. M. Gaudiosi, M. M. Murnane, and H. C. Kapteyn, "Unified microscopic-macroscopic formulation of high-order difference-frequency mixing in plasmas," Phys. Rev. Lett. **98**(4), 043903 (2007).
53. X. Zhang, A. L. Lytle, T. Popmintchev, X. Zhou, H. C. Kapteyn, M. M. Murnane, and O. Cohen, "Quasi-phase-matching and quantum-path control of high-harmonic generation using counterpropagating light," Nat. Phys. **3**(4), 270–275 (2007).
54. D. Popmintchev, C. Hernández-García, F. Dollar, C. Mancuso, J. A. Pérez-Hernández, M.-C. Chen, A. Hankla, X. Gao, B. Shim, A. L. Gaeta, M. Tarazkar, D. A. Romanov, R. J. Levis, J. A. Gaffney, M. Foord, S. B. Libby, A. Jaron-Becker, A. Becker, L. Plaja, M. M. Murnane, H. C. Kapteyn, and T. Popmintchev, "Ultraviolet surprise: Efficient soft x-ray high-harmonic generation in multiply ionized plasmas," Science **350**(6265), 1225–1231 (2015).
55. C. Hernández-García, J. A. Pérez-Hernández, J. Ramos, E. C. Jarque, L. Roso, and L. Plaja, "High-order harmonic propagation in gases within the discrete dipole approximation," Phys. Rev. A **82**(3), 033432 (2010).
56. T. Popmintchev, M.-C. Chen, D. Popmintchev, P. Arpin, S. Brown, S. Alisauskas, G. Andriukaitis, T. Balciunas,

O. D. Mücke, A. Pugzlys, A. Baltuska, B. Shim, S. E. Schrauth, A. Gaeta, C. Hernández-García, L. Plaja, A. Becker, A. Jaron-Becker, M. M. Murnane, and H. C. Kapteyn, "Bright coherent ultrahigh harmonics in the keV x-ray regime from mid-infrared femtosecond lasers," Science **336**(6086), 1287–1291 (2012).
57. X. Zhang, A. R. Libertun, A. Paul, E. Gagnon, S. Backus, I. P. Christov, M. M. Murnane, H. C. Kapteyn, R. A. Bartels, Y. Liu, and D. T. Attwood, "Highly coherent light at 13 nm generated by use of quasi-phase-matched high-harmonic generation," Opt. Lett. **29**(12), 1357–1359 (2004).
58. C. Hernández-García, T. Popmintchev, M. M. Murnane, H. C. Kapteyn, L. Plaja, A. Becker, and A. Jaron-Becker, "Group velocity matching in high-order harmonic generation driven by mid-infrared lasers," New J. Phys. **18**(7), 073031 (2016).
59. M. Ammosov, N. Delone, and V. Krainov, "Tunnel ionization of complex atoms and of atomic ions in an alternating electromagnetic field," Zh. Eksp. Teor. Fiz. **91**, 1191 (1986).
60. H. M. Milchberg, C. G. Durfee 3rd, and T. J. McIlrath, "High-order frequency conversion in the plasma waveguide," Phys. Rev. Lett. **75**(13), 2494–2497 (1995).
61. B. L. Henke, E. M. Gullikson, and J. C. Davis, "X-ray interactions: photoabsorption, scattering, transmission, and reflection at E=50-30000 eV, Z=1-92," At. Data Nucl. Data Tables **54**(2), 181–342 (1993).

## 1. Introduction and background

High harmonic generation (HHG) is an extreme nonlinear optical process, producing bright ultrashort bursts of laser-like extreme ultraviolet and soft x-ray beams in a tabletop-scale apparatus [1–5]. HHG is an ideal source for many applications, including nanoscale imaging [6], studies of nanoscale transport [7], ultrafast photoelectron spectroscopy [8–12], and element specific characterizations of ultrafast dynamics [13–17].

Traditionally, a single linearly polarized laser is used to drive the HHG process, producing linearly polarized high harmonic beams. Recent breakthroughs using either collinear or noncollinear counter-rotating circularly polarized driving lasers has enabled the production of high harmonic beams with controllable polarization, including fully circularly polarized HHG [18–28]. The noncollinear geometry enables the generation of angularly separated circularly polarized high harmonics [28], the production of linearly [29,30] or circularly polarized [31,32] isolated attosecond bursts, and the separation of harmonic orders without the use of a spectrometer [28,33]. Moreover, the emitted harmonics can be spatially separated from the fundamental driving laser beams [34–36], allowing samples to be placed close to the generation region, where the harmonic fluence is high, without being damaged by the driving laser. Previous investigations of noncollinear HHG have also probed the nonlinear optics of the HHG process [37] and shown that this is a promising geometry for cavity-assisted HHG [38–40]. Other work has used the noncollinear geometry to produce spectrally narrow EUV light [41] and applied a noncollinear probe beam to spatially and temporally characterize attosecond pulses [42]. While it provides new opportunities, a fundamental drawback of noncollinear HHG is that it provides a limit to the interaction length over which harmonics can be produced, which could result in a reduction in harmonic flux when compared to other geometries.

Due to the angular separation between the driving laser beams, phase-matching in noncollinear HHG [41,43] is fundamentally different from either single-beam HHG or collinear HHG [3,24,44–47] and presents both new challenges and new opportunities. Previous investigations of noncollinear HHG have shown that phase matching effects can determine the angle of preferential harmonic emission and used this angular dependence to infer the difference in the magnitude of the harmonic and driving laser wavevectors [43]. In this work, we experimentally and theoretically investigate the macroscopic physics of phase-matched noncollinear HHG at high pressures. First, we experimentally demonstrate phase matching of noncollinear HHG at ionization levels above critical ionization for the first time– which is normally the maximum ionization fraction at which full phase matching is possible in HHG. This capability is important because phase matching above critical ionization makes it possible to use higher driving laser intensities to produce bright higher-energy harmonics through the extension of the phase matched cutoff for a given wavelength driving laser. Second, we broadly explore the role of pressure in phase matching noncollinear HHG and show that the high pressures necessary to phase match noncollinear HHG mitigate the shortened interaction length in this geometry so that in many situations the flux can be identical to that produced in traditional HHG. Third, we extend the production of bright noncollinear highly elliptically polarized harmonics to photon energies of 90 eV, nearly doubling those obtained in previous studies [28]. Finally, we demonstrate the angular separation of high harmonic orders due to the noncollinear geometry of the generation process, removing the need for a spectrometer and therefore avoiding the associated losses.

In our experiment, we generate noncollinear HHG by overlapping two focused 790-nm pulses (45 fs) in a 100-μm-diameter gas jet with an adjustable angle between them (see Appendix A). These driving laser pulses are both either linearly polarized or circularly polarized with opposite helicity, producing either linearly or circularly polarized harmonics, respectively. When the driving lasers are linearly polarized there is no restriction on the number of photons from each beam contributing to the HHG process, as long as the total number of photons involved is odd to conserve parity [22]. This allows for many different channels of both high-order-sum-frequency generation (HOSFG, Fig. 1b) and high-order-difference-frequency generation (HODFG, Fig. 1c). Alternatively, when the driving lasers are circularly polarized with opposite helicity conservation of angular momentum requires that the number of photons absorbed from each beam only differ by ± 1, limiting the HHG process to two channels of HOSFG. In both cases, due to conservation of linear momentum, each allowed channel results in harmonic emission into a specific angle, given by

$$\tan\left(\theta_q\right) = \Delta m \tan\left(\theta_1\right) / q, \tag{1}$$

where $2\theta_1$ is the angular separation between the fundamental driving beams, $q$ is the harmonic order, and $\Delta m$ is the difference in the number of photons absorbed from each beam. HOSFG corresponds to $|\Delta m| < q$, while HODFG corresponds to $|\Delta m| > q$.

This angular dependence in the harmonic emission is advantageous because it spatially separates the high harmonics both from each other and from the fundamental driving lasers. Additionally, the angular dependence fundamentally changes the relationship between the phase velocity of the harmonics and the phase velocity of the driving laser. This change is important because the production of bright high harmonic beams requires phase matched frequency upconversion. Phase matching is achieved when there is no wave vector mismatch between the driving lasers and the emitted harmonics ($\Delta\vec{k} = 0$), such that harmonics generated at different spatial locations add coherently. In a collinear geometry, a scalar comparison of the wavevectors is sufficient (Fig. 1d). However, in a noncollinear geometry we must consider the *projection* of the driving laser wave vectors along the direction of the harmonic emission due to the angular differences between them (Fig. 1e-f) [28,43,48–50]. This projection results in a modified phase-matching equation:

$$\Delta k = m_A k_A \cos(\theta_1 - \theta_q) + m_B k_B \cos(\theta_1 + \theta_q) - k_q\,, \tag{2}$$

where $k_q$ is the wave vector of the emitted harmonic radiation, $k_A$ and $k_B$ are the driving laser wave vectors, and $m_A$ and $m_B$ are the number of photons absorbed from each beam respectively. Here, each wave vector includes the frequency-dependent bound- and free-electron contributions to the refractive index of the medium ($n_{\text{neutral}}$ and $n_{\text{plasma}}$ respectively, see Appendix B). While the refractive index of the medium for the harmonic light is close to one ($k_q \approx 2\pi/\lambda$), the refractive index at the driving laser frequency is increased in the presence of bound electrons and decreased in the presence of free electrons [3,44], i.e. $n_{\text{neutral}} > 1$ and $n_{\text{plasma}} < 1$. Additionally, as the crossing angle $\theta_1$ is increased, the noncollinear projection provides an increasing geometry-dependent phase mismatch that is negative for HOSFG and positive for HODFG (Fig. 1b, c). Therefore, phase matching must be accomplished by balancing this large noncollinear phase mismatch with the correspondingly large pressure dependent contributions to the refractive index from the bound or free electrons.

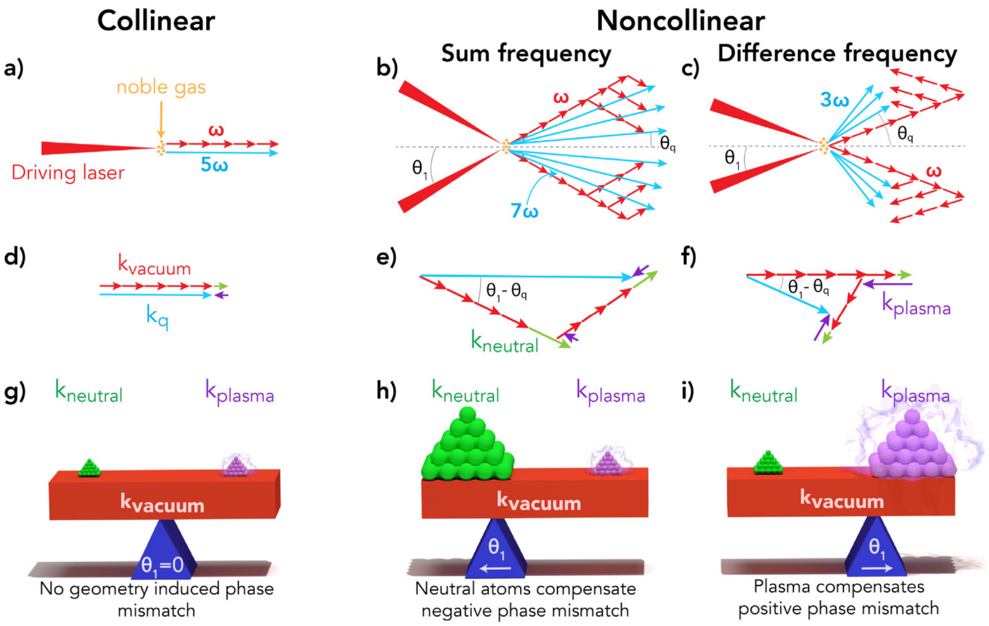

Fig. 1. Macroscopic physics of collinear and noncollinear high harmonic generation (HHG). In collinear HHG, the driving laser and emitted harmonics propagate in the same direction (a), so that there is no angle induced phase mismatch between the vacuum wave vectors (d) and the neutral and plasma contributions to the phase mismatch can primarily balance each other to phase match the process. (g). Conversely, in noncollinear HHG, two intense femtosecond lasers are overlapped in a gas jet at an angle $2\theta_1$. High harmonic beams are emitted at angles $\theta_q$, which are determined by conservation of energy and momentum. For high-order-sum-frequency mixing (HOSFG), the harmonic beams are emitted at smaller angles than the driving lasers (b), while for high-order-difference-frequency mixing (HODFG), the harmonic beams are emitted at larger angles (c). The difference in propagation direction introduces an angle-dependent contribution to the phase mismatch that is negative for HOSFG (e) and positive for HODFG (f). This phase mismatch must be balanced by either a large neutral contribution in HOSFG (h) or a large plasma contribution in HODFG (i).

The bound- and free-electron contributions to the refractive index are of opposite sign, and both scale linearly with the pressure in the interaction region, while their relative magnitude is determined by the ionization fraction ($\eta$). The ionization fraction at which the bound- and free-electron dispersions are equal is known as the critical ionization level ($\eta_c \approx 0.5\%$ for He with 800 nm) [3,44]; here the phase mismatch due to the electrons bound in neutral atoms cancels that of the free-electron plasma. Typically, critical ionization places an upper limit on the laser intensities that can be used to drive HHG because at ionization levels above $\eta_c$, the free-electron contribution to the index dominates, resulting in a driving laser phase velocity much greater than $c$ [51,52]. Exceptions to this rule include quasi phase matching [53] or UV-driven HHG, where bright HHG beams can be produced through effective phase matching in multiply-ionized plasmas [43].

In noncollinear HHG, phase matching requires a balance between the pressure dependent bound- and free-electron dispersions and the geometry dependent phase mismatch from the noncollinear projection. Here, the geometry-dependent phase mismatch has different consequences for HOSFG and HODFG. In HOSFG a large (positive) neutral contribution is required to balance the negative phase mismatch from the noncollinear projection (Fig. 1h). Conversely, in HODFG a large (negative) plasma contribution is needed to balance the positive phase mismatch induced by the noncollinear projection (Fig. 1i). Note that regardless of the specific conditions, the noncollinear phase mismatch varies as the cosine of the angular separation between the emitted harmonics and the driving lasers, which behaves quadratic in the small angle approximation [43] (see Appendix B, Fig. 6).

## 2. Results

### A. Phase matching in a noncollinear geometry

To experimentally investigate the angular dependence of phase matching in a noncollinear geometry we measure the high harmonic flux as a function of the gas pressure in the generation region (either Xe or Ar, see Appendix C). The harmonic flux is maximized at the pressure that fully phase matches the HHG process (see Appendix D) [44,45]. We probe this phase-matching pressure using linearly polarized driving lasers, taking advantage of the many high harmonic beams emitted at many different angles simultaneously (Fig. 2a) through both HOSFG and HODFG. Additionally, we investigate phase matching both above and below critical ionization ($\eta \approx 4\eta_c$ and either $0.25\eta_c$ or $0.99\eta_c$ respectively), where these two distinctly different regimes exhibit different angular dependencies of the phase matching pressure (Fig. 2b).

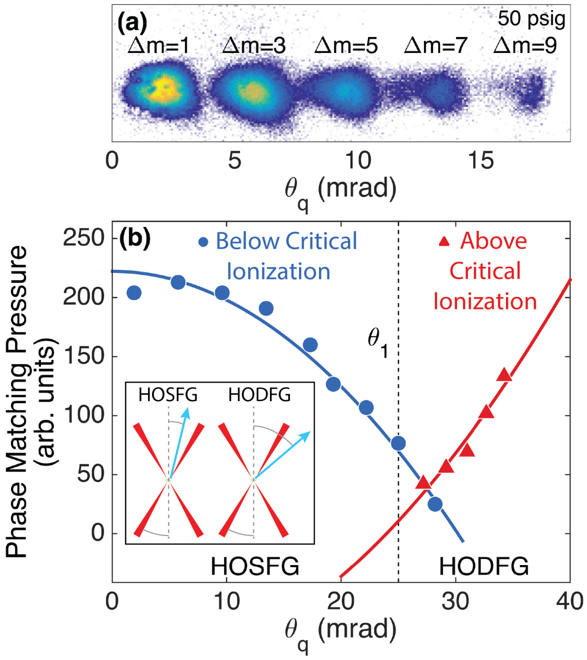

Fig. 2. Experimental phase-matching pressure measurements. (a) Raw camera image showing HHG beams emitted into several different angles, $\theta_q$, due to the absorption of different numbers of photons from each driving beam ($\Delta m$). We monitor the flux in each HHG emission angle as a function of the gas jet backing pressure to measure the angular dependence of the phase-matching pressure. (b) Phase-matching pressure as a function of harmonic-emission angle measured both above and below critical ionization; the angle of the driving laser, $\theta_1$, as shown in the inset, is indicated by the vertical-dashed line. The noncollinear geometry results in a negative phase mismatch for HOSFG and a positive phase mismatch for HODFG, which increases in magnitude with increasing angular separation from the fundamental driving laser. Below critical ionization (blue circles, Xe, $\eta \approx 0.25\eta_c$ and $0.99\eta_c$), HOSFG requires higher pressures to compensate this geometric factor and HODFG requires lower pressures. The increase in phase matching pressure is more pronounced for harmonics with larger angular separation from the driving laser. Conversely, the opposite behavior is seen above critical ionization (red triangles, Ar, $\eta \approx 4\eta_c$). The solid lines are the result of fitting the data to the expected $\theta_q^2$ dependence of the phase matching pressure. The experimental data points are measured at three different experimental conditions (see Appendix C, Fig. 7).

Below critical ionization, the phase mismatch due to the neutral and plasma dispersion is positive and increases with increasing pressure. Consequently, increasingly high pressures can compensate the negative phase mismatch due to the noncollinear projection in HOSFG. This results in higher phase matching pressures for larger angular separations between the emitted harmonics and the driving laser beams (Fig. 2b, blue curve). Therefore, this increase in phase-matching pressure is especially important for larger angular separation between the driving lasers and circularly polarized noncollinear HHG. Although challenging to achieve, high gas pressures increase the number of emitters, which produces brighter harmonic emission (up to absorption limited lengths [44,45]). Therefore, the high pressures required for phase matching noncollinear HOSFG help to counter the decrease in harmonic flux arising from the shortened interaction length as compared to the length attainable in single-beam or collinear HHG.

Above critical ionization, the phase mismatch due to the neutral and plasma dispersion is negative. In this case, higher pressures provide a more negative phase mismatch, which compensates the positive noncollinear phase mismatch in HODFG (Fig. 2b, red curve). Therefore, the observation of increasing phase-matching pressures for HODFG with increasing angular separation from the driving lasers is a clear signature of phase matching above critical ionization.

To provide further evidence of HODFG phase matching above critical ionization we perform numerical simulations of HHG including propagation using a method based on the electromagnetic field propagator (see Appendix E) [55]. In these simulations, as in the experiment, two linearly polarized beams are crossed at an angle ($\theta_1$ = 25 mrad) to drive high harmonic generation, producing high harmonics that are angularly dispersed (Fig. 3a). Comparing the simulated HHG yield at different pressures allows us to numerically investigate the role of phase matching in a noncollinear geometry. If the HHG process is equally well phase matched at all pressures then the harmonic intensity will scale as the pressure squared; deviations from that scaling indicate more or less efficient phase matching. The driving laser pulses are modeled so the ionization fraction in the interaction region is above critical ionization ($\eta = 2\eta_c$) at the peak of the pulse. Consequently, the pressure scaled harmonic yield for HOSFG decreases with increasing pressure. Conversely, the pressure scaled harmonic yield for HODFG either remains unchanged (one photon of DFG) or increases (two photons of DFG) for increasing pressures, indicating that HODFG is well phase matched above critical ionization and HOSFG is not (Fig. 3b). The ability to phase-match above critical ionization provides the opportunity to drive the HHG process with more pulse energy than is possible for single-beam or collinear HHG, producing higher energy harmonics.

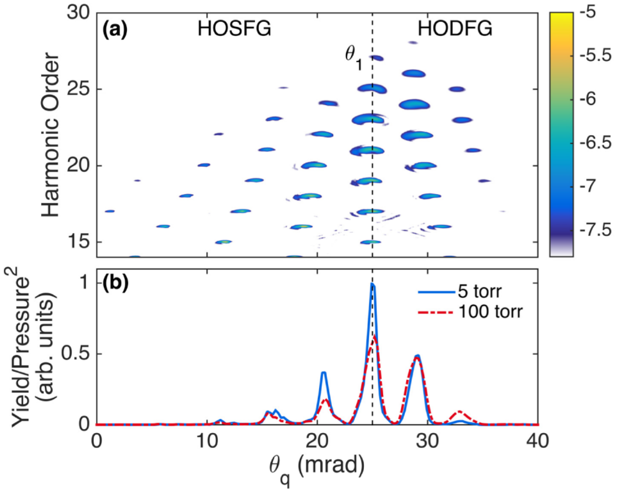

Fig. 3. Numerical simulations of noncollinear high harmonic generation above critical ionization ($\eta = 2\eta_c$) in an argon gas jet. (a) Harmonics are emitted into many different angles corresponding to both HOSFG and HODFG. Note the presence of even harmonic orders because this simulation uses a 790 nm and a 395 nm driving beam (see Appendix E); here harmonic order is denoted with respect to the 790 nm beam. The harmonic intensity is shown on a log scale. (b) The integrated harmonic yield as a function of harmonic emission angle is dependent on the pressure. If the phase matching efficiency is unchanged then the yield will scale as the pressure squared, therefore differences in the pressure-normalized yield are due to phase matching. Comparison of low (solid blue) and high (dashed red) pressure shows that HOSFG is not well phase matched above critical ionization but HODFG is. Here, the lines correspond to integrating the 21st harmonic order and above.

### *B. Generation of circularly polarized noncollinear high harmonics above 90 eV*

Now that we have verified our model of phase matching in a noncollinear geometry, we can apply that understanding to produce noncollinear highly elliptically polarized high harmonics. In HHG with circularly polarized counter-rotating driving lasers the conservation of spin angular momentum limits the difference in the number of photons absorbed from each beam to $\Delta m = \pm 1$. Therefore, the suppression of any HHG channels corresponding to higher values of $\Delta m$ indicates that the remaining HHG emission is either circularly or highly elliptically polarized [26]. We produce highly elliptically polarized high harmonics up to 90 eV (Fig. 4), which is almost double the photon energies previously obtained using this technique [28]. We achieve these photon energies by modifying our experimental chamber to accommodate higher gas flow rates that result from increasing the pressure in the generation region and by using helium as the HHG medium. In single-beam HHG, higher-energy harmonics are produced by increasing the ionization potential of the HHG medium or increasing the wavelength of the driving laser [3,44,54,56,57]. However, both of these approaches require increasingly high phase-matching pressures. In the noncollinear geometry, these effects are compounded by the geometry-dependent phase mismatch because the production of circularly polarized harmonics with counter-rotating driving lasers is an HOSFG process. Here, only HOSFG processes (with $\Delta m = \pm 1$) are possible because HODFG processes would result in photons with a large and therefore forbidden spin angular momentum. Consequently, to favor HOSFG, the ionization fraction was maintained below the critical ionization level. As demonstrated here, the challenge of phase matching high energy circularly polarized noncollinear HHG can be overcome with a full understanding of the phase-matching conditions in this geometry.

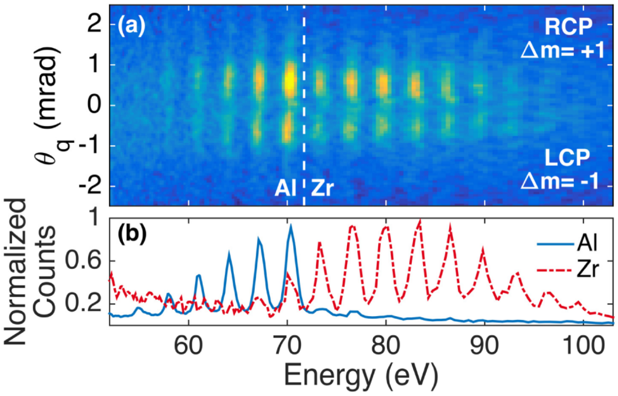

Fig. 4. Circularly polarized noncollinear HHG in excess of 90 eV. (a) The angularly resolved spectrum obtained through noncollinear HHG in helium with circularly polarized driving lasers shows two circularly polarized harmonic beams with right and left circular polarization, respectively, at positive and negative divergence angles. (b) The angularly integrated spectrum shows high-order harmonics that extend to energies above 90 eV. An aluminum (Al) filter is used to isolate the low-energy portion of the spectrum (blue solid line) and a zirconium (Zr) filter is used to isolate the high-energy portion (red dashed line).

The high-energy harmonics from He (Fig. 4) are generated with usable flux (~$10^6$ photons/sec/harmonic above the aluminum edge at ~70 eV, see Appendix G). We note that this flux is an order of magnitude lower than the flux that has been attained in high energy collinear circularly polarized HHG (~$5\times10^7$ photons/sec/harmonic [26]). This difference is due to the difficulty in implementing very high pressures in the gas jet geometry required for noncollinear HHG and therefore the difficulty in achieving the maximum absorption limited HHG flux. Therefore, in the future, further increasing the gas pressure could result in even brighter harmonics because of a favorable phase matching pressure scaling, which mitigates the decrease in interaction length due to the finite overlap region between the two beams. This can be understood by considering the crossing angle dependence of the pressure-length-product – in the small angle approximation the length of the overlap region between the two beams decreases linearly as $\theta_1$ is increased but the phase matching pressure increases quadratically with $\theta_1$ (see Appendix B). Consequently, the phase-matched pressure-length-product actually increases linearly with increasing noncollinear crossing angle. In the case where the flux is limited by the length of the interaction region, for example by the extent of the gas jet, we would expect the flux generated by a noncollinear geometry to exceed that obtained in the collinear geometry. In the case where significant re-absorption of the harmonic light takes place, as in the commonly encountered absorption limited regime, noncollinear and collinear HHG should produce identical flux. However, we emphasize that the pressure required for phase matching noncollinear HHG increases dramatically with angle, as well as with the wavelength of the driving laser and the ionization potential of the gas species, quickly reaching many atmospheres. Moreover, to avoid re-absorption of the harmonic light, the pressure must quickly transition to high vacuum, presenting a formidable design challenge.

### *C. Angular separation of high harmonics without a spectrometer*

Finally, we use our understanding of noncollinear phase matching to achieve spatial separation between different high harmonic orders without the use of a spectrometer. This spatial separation is possible in a noncollinear geometry because the angle at which harmonics are emitted, $\theta_q$, depends on the harmonic order. Separating the harmonic orders in the far field requires that the difference in $\theta_q$ between adjacent harmonic orders be larger than the divergence of the high harmonics. Previous studies have shown the separation of low-order harmonics (3rd and 5th) in circularly polarized noncollinear HHG [28]. Here, we extend this technique to demonstrate a clear spatial separation of higher harmonic orders (13th and 15th) in the far field (Fig. 5a). We do so with linearly polarized noncollinear HHG, which allows for the use of a larger $\Delta m$ to increase the angular spread between adjacent harmonic orders (Eq. (1)).

As we increase the pressure in the interaction region harmonics emitted with larger angular separation from the driving lasers, and therefore with smaller $\theta_q$, are preferentially phase matched (Fig. 5b-c). Therefore, we can use pressure tuning to favor harmonic emission at a particular angle corresponding to bright harmonic emission of the 13th and 15th harmonic orders, produced through HOSFG with $\Delta m = 7$. At these harmonic emission angles the 13th and 15th harmonic orders are well separated, demonstrating the spatial separation of high harmonic orders in the far field without a spectrometer. In this case the laser intensity is chosen so that very little of the next harmonic order is produced. If the 17th harmonic order was present it could not be similarly separated without increasing either $\Delta m$ or the angle between the fundamental driving beams (see Appendix H, Fig. 10). Consequently, this technique can only be applied to achieve complete angular separation without a spectrometer in a situation where a small number of harmonic orders are produced, but in general provides an easily tunable spatially varying energy distribution.

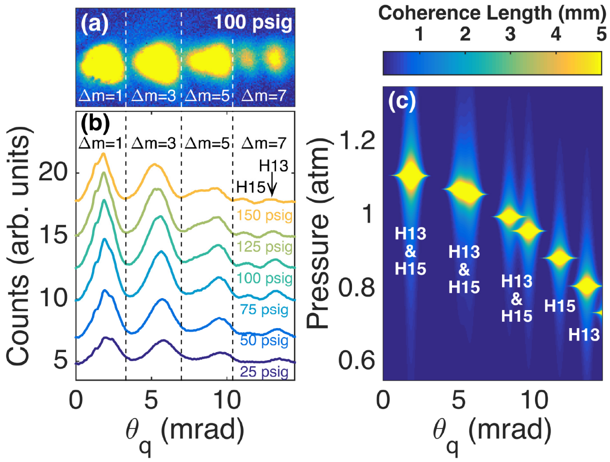

Fig. 5. Angular separation of high harmonic orders without a spectrometer. (a) At higher pressures, the raw camera image clearly shows two spatially separated peaks on the right hand side, corresponding to the 13th and 15th harmonic orders produced through HOSFG with $\Delta m = 7$. (b) Spatial distribution of harmonic flux with increasing gas-jet backing pressure, vertically displaced for clarity. The peak that grows in between the main $\Delta m = 5$ and 7 peaks corresponds to the 15th harmonic order, which is spatially separated from the 13th harmonic order. (c) Spatial separation of high harmonic orders in the far field is only possible if the difference in the emission angle of adjacent harmonic orders is larger than the divergence of the harmonics themselves. The theoretical coherence length of harmonic emission as a function of pressure and $\theta_q$ shows pressures where this can be achieved and bright well-separated emission of the 13th and 15th harmonic orders is attained.

## 3. Conclusions

In summary, noncollinear HHG is an emerging technique that can be used to produce angularly separated circularly polarized high harmonics, generate isolated attosecond bursts, and separate high harmonic orders from both each other and the fundamental driving lasers. However, to fully harness HHG in a noncollinear geometry, a complete understanding of the phase matching is necessary. We showed that phase matching HOSFG requires increasingly high pressures in the interaction region, which has important experimental consequences for the production of high-energy circularly polarized high harmonics. These increased phase matching pressures are technically challenging to achieve but offset the decrease in flux due to the shortened interaction region in a noncollinear geometry. Additionally, we demonstrated phase matching above critical ionization using HODFG, which enables higher driving laser intensities to produce higher energy harmonics than are attainable in single-beam HHG. Next, we used our understanding of phase matching in this noncollinear geometry to produce noncollinear highly elliptically polarized high harmonics in excess of 90 eV, extending the energy range over which this technique is useful for studying circular dichroism. Finally, we demonstrated angular separation of high harmonic orders without the use of a spectrometer, which is experimentally advantageous because EUV optics are difficult to fabricate and can exhibit high loss. Further experiments may extend noncollinear HHG to produce noncollinear circularly polarized harmonics at even higher energies and to generate circularly polarized isolated attosecond bursts.

## Appendix A: Experimental details

Experimentally, we investigate noncollinear HHG by crossing two focused laser pulses into a gas jet. These pulses originate from a Ti:Sapphire amplifier (Wyvern HE, KM Labs), which provides 8 mJ pulses, centered at 790 nm, with 45 fs pulse durations at a 1 kHz repetition rate. These pulses are split into two arms, which are overlapped in time using a delay stage placed in one of the arms. The polarization in each arm is controlled with a half- and quarter-wave plate pair and the intensity in each arm is controlled with a half-wave plate and polarizer pair. The two arms travel parallel to each other into the final focusing lens, which focuses both arms to the same point, overlapping them in space with an adjustable angle between them. The pulses are focused into a gas jet with a diameter of 100 μm to drive the HHG process in xenon, argon, or helium.

For most of the measurements presented here, we used 790-nm laser beams in both arms. However, in some cases we mix the fundamental in one arm with the second harmonic (395 nm) in the other by placing a β-barium borate crystal (200 μm thickness) in one of the arms.

## Appendix B: Functional dependence of the noncollinear wave vector mismatch and phase matching pressures

The production of bright harmonic beams requires phase matching the HHG process [44]. Phase matching is achieved when there is no wave vector mismatch between the driving laser and the emitted harmonics, $\Delta\vec{k} = q\vec{k}_1 - \vec{k}_q = 0$, where $q$ is the harmonic order and $\vec{k}_1$ and $\vec{k}_q$ are the wave vectors of the fundamental and high harmonics respectively. The index of refraction of the medium at extreme ultraviolet wavelengths is typically very close to one, such that $k_q = 2\pi / \lambda_q$, where $\lambda_q$ is the high harmonic wavelength. However, the index of refraction of the medium at the driving laser wavelengths is modified by the presence of both bound and free electrons, so that

$$\begin{aligned} k_1 &= k_{\text{vacuum}} + k_{\text{neutral}} + k_{\text{plasma}} + \ldots, \\ k_{\text{vacuum}} &= 2\pi / \lambda_1, \\ k_{\text{neutral}} &= \left(\tfrac{2\pi}{\lambda_1}\right)(n-1)(1-\eta)P, \\ k_{\text{plasma}} &= -r_e N_{\text{atm}} \lambda_1 \eta P. \end{aligned} \tag{3}$$

Here, $n$ is the index of refraction of the neutral gas, $r_e$ is the classical electron radius, $N_{\text{atm}}$ is the number density of atoms in an atmosphere of gas at standard temperature and pressure, $\eta$ is the ionization fraction, and $P$ is the pressure in atmospheres [44]. Both $k_{\text{neutral}}$ and $k_{\text{plasma}}$ increase in magnitude with increasing pressure and their relative size is determined by the ionization fraction. The ionization fraction at which they are equal is known as critical ionization ($\eta_c$). Therefore, below critical ionization the combined $k_{\text{neutral}} + k_{\text{plasma}}$ leads to a positive phase mismatch and above critical ionization it leads to a negative phase mismatch, which increases in magnitude with increasing pressure in both cases. There are also geometric terms (represented by the ellipsis in Eq. (3)) that modify the driving laser wave vector, such as the Gouy phase and the atomic dipole terms. However, these terms are independent of the pressure and ionization fraction and are small compared to the effect of the noncollinear angle.

For example, with 790-nm driving lasers and a separation of $\theta_1$ = 25 mrad the phase mismatch due to the noncollinear projection at $\theta_q$ = 0 is of order $10^4$ $m^{-1}$. At typical experimental conditions, we estimate the magnitude of the phase mismatch due to the Gouy phase shift to be of order $10^3$ $m^{-1}$, which is an order of magnitude smaller than the size of the noncollinear phase mismatch. Similarly, across the experimental conditions employed here the atomic dipole term ranges from approximately $10^2$ to $10^3$ $m^{-1}$, which is again much smaller than the effects of the noncollinear projection. In general, this phase mismatch introduced by the noncollinear geometry dominates because it corresponds to a projection of the full vacuum wave vectors, which are large (~$10^6$ $m^{-1}$). Consequently, even a small angle will have a large effect on the phase matching conditions.

In the noncollinear geometry, there is a difference in the propagation angle of the driving lasers ($\theta_1$) and the emitted harmonics ($\theta_q$). Therefore, we must consider the projection of the driving laser wave vector along the direction of the high harmonic wave vector,

$$\Delta k = m_A k_A \cos(\theta_1 - \theta_q) + m_B k_B \cos(\theta_1 + \theta_q) - k_q\,, \tag{4}$$

where $k_A$ and $k_B$ are the driving laser wave vectors and $m_A$ and $m_B$ are the number of photons absorbed from each beam respectively [28,43]. Because each of the wave vectors can be broken into individual components (vacuum, neutral, plasma, etc) the noncollinear phase mismatch can also be broken into pressure independent (vacuum phase mismatch) and pressure dependent portions. The pressure independent portion is given by

$$\Delta k_{\text{vac}} = m_A \frac{2\pi}{\lambda_A}\cos(\theta_1 - \theta_q) + m_B \frac{2\pi}{\lambda_B}\cos(\theta_1 + \theta_q) - \frac{2\pi}{\lambda_q}, \tag{5}$$

where $\lambda_A$ and $\lambda_B$ are the wavelengths of the driving lasers and $\lambda_q$ is the harmonic wavelength (Fig. 6a). This projection gives a $(\theta_1 \pm \theta_q)^2$ dependence in the small angle approximation. The remaining portion of the wave vector mismatch is linearly dependent on pressure, so that the pressure at which $\Delta k = 0$ (Fig. 6b) will scale according to the pressure independent phase mismatch, with a $\theta_q^2$ dependence (since $\theta_1$ is fixed here). Different ionization fractions will require a different absolute phase matching pressure but will maintain the same functional form of the angular dependence (Fig. 6b).

Including the effect of the Gouy phase and atomic dipole terms in this analysis provides an additional pressure independent phase mismatch that is essentially angularly independent. These terms will uniformly increase or decrease the noncollinear phase mismatch by some amount but leave the angular dependence unchanged. Consequently, the phase matching pressures would be slightly shifted but the quadratic dependence on $\theta_q$ remains. In the case where the two input beams share the same linear polarization, there are strong intensity modulations resulting from interference. These modulations in the driving field lead to a grating-like harmonic source term [28]. Additionally, the modulations in the driving field strength lead to a similar grating-like structure in the atomic dipole phase. However, due to the high nonlinearity of the HHG process harmonics are only produced in the regions of highest intensity, over which the variation in the atomic dipole term is minimal. Therefore, the strong intensity and quantum phase modulations present in this situation do not affect the phase matching but they will tend to push more power into higher diffracted orders, i.e. large $\Delta m$.

We note that Eq. (5) ignores the effect of $k_{\text{neutral}}$ and $k_{\text{plasma}}$ on $\theta_q$. However, the vacuum wave vectors are so much larger than the neutral and plasma contributions that although the latter terms are important for phase matching they make only a negligible contribution to the angle of harmonic emission for the conditions explored in this study.

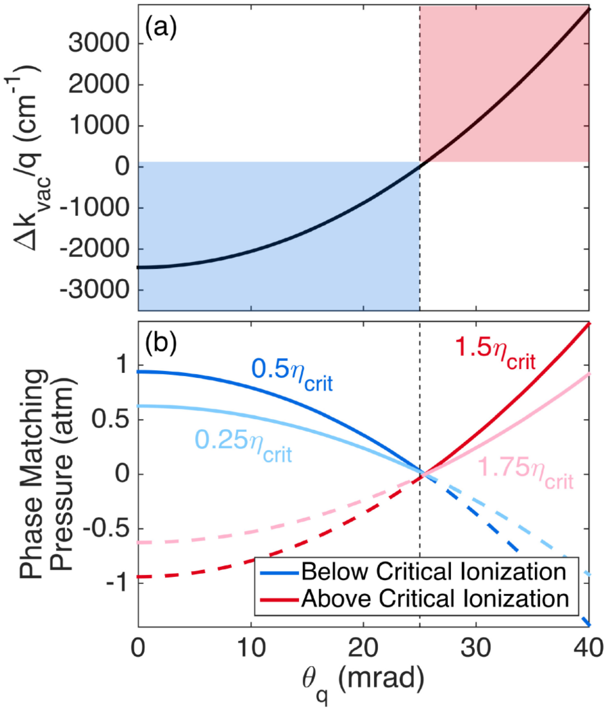

Fig. 6. Theoretical angular dependence of the phase matching of noncollinear high harmonic generation (HHG) in xenon with a driving laser angular separation with half-angle $\theta_1 = 25$ mrad (vertical dashed line). (a) The wave vector mismatch as a function of harmonic emission angle is negative for HOSFG and positive for HODFG. (b) Pressure tuning is used to balance the geometry-dependent phase mismatch, resulting in phase matching pressures that increase with increasing angular separation from the driving laser. The sign of the pressure dependent phase matching term is dependent on the ionization fraction of the medium, so HOSFG is phase matched below critical ionization (blue) because the positive pressure dependent terms balance the negative noncollinear phase mismatch (blue region in (a)). Conversely, HODFG is phase matched above critical ionization (red), where the negative pressure dependent terms balance a positive noncollinear phase mismatch (red region in (a)). Different experimental conditions (light and dark curves) change the absolute scaling of the phase matching pressure but the angular dependence maintains the functional form of the wave vector mismatch. Dashed lines indicate regions where phase matching is experimentally unachievable because the required pressures are negative.

## Appendix C: Absolute phase matching pressures at different experimental conditions

Practically, it is not possible to map out the entire angular dependence of the phase matching pressure using a single set of experimental conditions. Obviously, both above and below critical ionization cannot be probed simultaneously. However, even when exploring the phase matching pressure below critical ionization the harmonic emission at all HOSFG angles could not be measured at the same experimental conditions. This is because the harmonic emission angle that is statistically the most probable depends on the intensity ratio between the two driving beams [37]. When the two driving lasers are the same intensity harmonics are predominately emitted equally between the two lasers and therefore at small angles ($\theta_q \sim 0$). However, when one beam is more intense harmonics are preferentially emitted at angles near the more intense driving laser ($\theta_q \sim \theta_1$). Therefore, we used three different experimental conditions to map out the phase matching pressure at a wide range of harmonic emission angles, as well as above and below critical ionization. These different experimental conditions result in different absolute phase matching pressures (Fig. 7). However, regardless of the specific conditions the phase matching pressure goes as $\theta_q^2$. Therefore, the experimental pressures in Fig. 2 were scaled to emphasize the universal behavior of the phase mismatch.

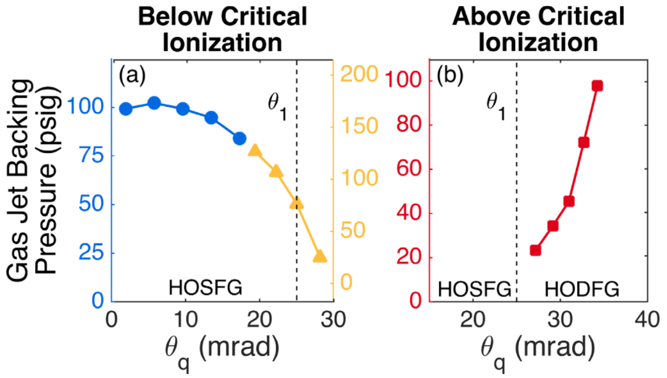

| (c) | Gas | $\lambda_1, \lambda_2$ (nm) | $\sim I_1/I_2$ | $\sim I_{tot}$ (W/cm$^2$) | $\sim \eta/\eta_{crit}$ |
|---|---|---|---|---|---|
| Blue Circles | Xe | 790, 790 | 1 | $7\times10^{13}$ | 0.25 |
| Yellow Triangles | Xe | 790, 790 | 10 | $9\times10^{13}$ | 0.99 |
| Red Squares | Ar | 395, 790 | 10 | $3\times10^{14}$ | 4 |

Fig. 7. Experimentally observed dependence of the phase-matching pressure on the emission angle. This data was collected at three different experimental conditions to fully explore the angular dependence of the phase matching pressure. (a) Two different experimental conditions were necessary below critical ionization to optimize harmonic emission at either small (blue circles) or large (yellow triangles) angles. (b) A single set of experimental parameters was used above critical ionization (red squares). (c) The relevant experimental parameters, where intensities are estimated from Gaussian beam optics.

## Appendix D: Angularly resolved scaling of the harmonic yield with gas jet pressure

To obtain the angularly dependent phase matching pressures (Fig. 2 and Fig. 7) we measure the angularly resolved harmonic yield as a function of the gas jet backing pressure with linearly polarized driving lasers. Without a spectrometer in place, we observe a series of harmonic beamlets on the camera, which correspond to the absorption of different numbers of photons from each driving laser (Fig. 8a). We note that because the angle of harmonic emission depends on the harmonic order, the fact that we see a series of discrete beamlets means that there are not very many harmonic orders present. When there are many harmonic orders present these beamlets merge and assignments can no longer be made without also spectrally dispersing the harmonics.

We record a series of these angularly resolved images at several different gas jet backing pressures. This allows us to find the phase matching pressure at many different harmonic emission angles simultaneously by observing the harmonic yield in each beamlet as a function of pressure (Fig. 8b-f). For each harmonic beamlet, there is a pressure at which the harmonic yield in that beamlet is maximized. This optimal pressure is due to phase matching effects [44,45] and therefore has an angular dependence due to the angularly varying phase mismatch that arises in a noncollinear geometry.

We obtained the $\theta_q$ axis by considering the number of photons absorbed from each beam and enforcing conservation of linear momentum (Eq. (1)), which has been previously shown to accurately predict the angles of harmonic emission in a noncollinear geometry [28]. For the conditions shown in Fig. 8a (blue circles in Fig. 7a) we observed primarily the 13th harmonic order with a small contribution from the 15th harmonic order. As a check, we used the $\theta_q$ axis obtained from Eq. (1) and the known pixel size of the CCD camera (Andor, DO420-BN) to calculate the distance from the gas jet to the camera to ensure that this procedure gives a physically reasonable result.

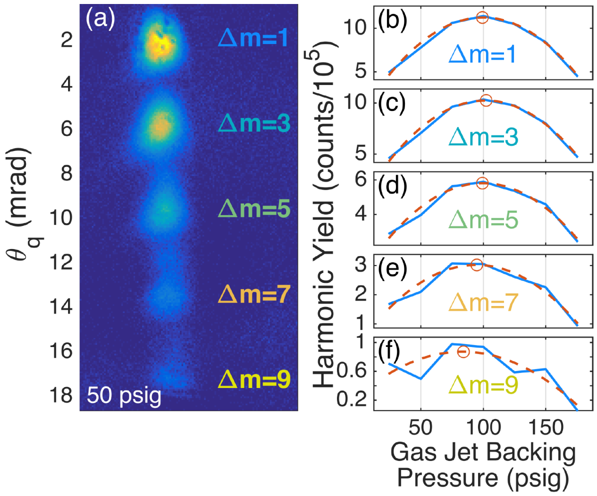

Fig. 8. Angularly resolved pressure dependence of harmonic yield. (a) The raw camera image shows several high harmonic beamlets emitted into different angles, which correspond to absorption of different numbers of photons from each driving laser beam ($\Delta m = 1,3,\ldots9$). (b-f) The yield in each high harmonic beamlet in (a) is measured as a function of the gas jet backing pressure (solid blue lines) to find the optimal pressure as a function of harmonic emission angle. As the pressure is increased the harmonic yield will increase until the pressure at which the phase matching is optimized (i.e. the phase matching pressure). After this point further increasing the pressure causes the harmonic yield to decrease. The phase matching pressure found for each harmonic beamlet is marked with a red circle. The dashed red lines are quadratic fits to the yield as a function of pressure.

## Appendix E: Theoretical methods

We compute HHG including propagation using a method based on the combination of the strong field approximation with the electromagnetic field propagator [55]. We discretize the target (gas jet) into elementary radiators, and propagate the emitted field $E_j(r_j,t)$ to the far-field detector,

$$E_j(r_j,t)=\frac{q_j s_d}{c^2\,|r_d-r_j|}\left[s_d\times a_j\left(t-\frac{|r_d-r_j|}{c}\right)\right], \tag{6}$$

where $q_j$ is the charge of the electron, $s_d$ is the unitary vector pointing to the detector, and $r_d$ and $r_j$ are the position vectors of the detector and of the elementary radiator $j$, respectively. The dipole acceleration $a_j$ of each elementary source is computed using an extension of the strong field approximation. The signal at the detector is computed as the coherent addition of the high harmonic contributions of all the elementary sources where the high harmonics are assumed to propagate to the detector with a phase velocity $c$, the speed of light. Propagation effects of the fundamental field, including plasma and neutral dispersion as well as time-dependent group velocity walk-off [58], are taken into account. We account for the time-dependent induced ionization population (computed via the instantaneous ADK rates [59]), thus including nonlinear phase shifts in the driving field. Nonlinear spatial effects are not taken into account. The absorption of the harmonics in the gas is modeled using Beer's law.

The simulation results presented in Fig. 3 of the main text are performed considering red (790 nm) and blue (395 nm) linearly polarized driving beams, which cross with a half angle of 25 mrad. The laser temporal pulse envelopes are modeled by a truncated $\sin^2$ function with pulse duration of 30 fs at full width half maximum (FWHM). Each non-collinear driving beam is assumed to have a Gaussian spatial profile with a beam waist at focus of 100 µm. The blue pulse exhibits 10% of the intensity of the red pulse, yielding a total peak intensity of $1.73\times10^{14}$ W/cm$^2$ at the focus position. These intensities result in an ionization fraction of 8% at the peak of the pulse, corresponding to $\eta = 2\eta_c$. Therefore, HODFG is well phase matched and HOSFG is not. The target is modeled as an argon gas jet flowing perpendicular to the longitudinal (laser propagation) direction, $z$. The gas jet profile is constant in the $x$ direction, while Gaussian in the $y$ and $z$ directions, with a FWHM of 100 µm, and peak pressures of 5 torr and 100 torr (Fig. 9). In the calculations shown in this work, the gas jet is placed 500 µm after the focus position.

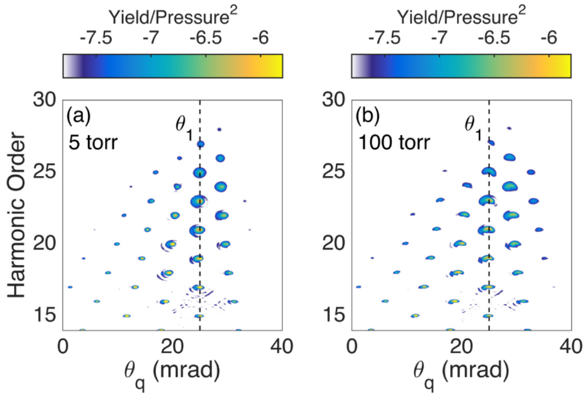

Fig. 9. Simulated angle resolved harmonic spectra from noncollinear HHG with linearly polarized beams. The driving beams are 790 nm and 395 nm and separated by a half angle of $\theta_1$ = 25 mrad. The 790-nm beam is 10 times more intense than the 395-nm beam and the vertical dashed line denotes its angle. The harmonic spectrum is displayed on a log scale and is normalized by the pressure squared. Simulations were conducted at two different pressures (a) 5 torr and (b) 100 torr. These laser conditions result in an ionization fraction above critical ionization ($\eta = 2\eta_c$), therefore HODFG is well phase matched and HOSFG is not. Consequently, the pressure normalized yield of the HODFG emission stays the same or increases as the pressure is increased.

## Appendix F: Critical ionization in two-color fields

Critical ionization is the ionization fraction at which the phase mismatch from the neutral and plasma terms are equal [3,44]. For ionization fractions above critical ionization phase matching cannot occur, which typically sets an upper limit on the intensities that can be used to drive HHG. In traditional one-color high harmonic generation it is a good approximation that the phase matching conditions are the same for all harmonic orders. Therefore, the critical ionization level is also the same for all harmonic orders and is given by

$$\eta_c = \left(1 + \frac{r_e N_{\text{atm}} \lambda^2}{2\pi(n-1)}\right)^{-1}. \quad (7)$$

However, in a two-color field the precise phase matching conditions, and therefore the critical ionization level, depends on the number of photons absorbed from each beam. In this case, the critical ionization level is given by,

$$\eta_c = \left(1 + \frac{r_e N_{\mathrm{atm}}}{\pi} \frac{\lambda_a{}^2 (m_a + m_b \lambda_b / \lambda_a)}{m_a(1-n_a) + m_b(1-n_b)\lambda_a / \lambda_b}\right)^{-1}, \tag{8}$$

where $m_\mathrm{a}$ and $m_\mathrm{b}$ are the number of photons absorbed from each beam respectively. In general, for HOSFG the critical ionization level in a two-color field is somewhere between the critical ionization level for each color independently. Conversely, for HODFG the critical ionization level is either lower than the critical ionization level for the longer wavelength driver or higher than the critical ionization level for the shorter wavelength driver depending on which wavelength photon is being subtracted. Interestingly, in certain regimes of two-color HODFG the critical ionization level can approach arbitrarily high levels. This is because the second term in Eq. (8) goes to zero when $m_a = -m_b\lambda_b / \lambda_a$, along the lines of an earlier proposal [60]. Therefore, two-color HODFG with a long wavelength driving field can dramatically increase the phase matched cutoff energy by allowing for much higher driving intensities.

In the two-color field cases explored in this work, one of the driving lasers was always much more intense than the other, resulting in harmonic emission that was due to absorption of the majority of photons from one of the beams and only one or two photons from the other beam. Therefore, the critical ionization level was essentially unchanged from the single-color critical ionization level of the dominant beam. In the experimental case (Fig. 7, red squares) the primary beam was 395 nm, corresponding to a critical ionization level of ~14%. In the numerical simulations, the primary beam was 790 nm, corresponding to a critical ionization level of ~3.8%. Both the experiment and numerical simulations were conducted in argon.

## Appendix G: High-energy circularly polarized HHG flux characterization

To characterize the experimental flux of high-energy circularly polarized harmonics produced in a noncollinear geometry we first record the angularly resolved harmonic spectrum with an EUV spectrometer (Hettrick Scientific) and a CCD camera (Fig. 4). We use two 200 nm thick zirconium filters to transmit the high-energy (>72 eV) portion of the harmonic spectrum while rejecting the fundamental driving laser light. By angularly and spectrally integrating the camera image we attain our high-energy harmonic flux in counts/second.

To convert from counts to photons we use the camera specifications supplied by the manufacturer for the electrons/count (~10), photons/electron (~1/20), and quantum efficiency (~87%). Since these vary over the energy range of our harmonic spectrum (72–100 eV), we used the values corresponding to the brightest portion of the spectrum (~80 eV). This gives the measured photons/pulse at the detector, however to estimate the number of photons/pulse emitted from the HHG source we must correct for the loses upon transmission through the two zirconium filters and the spectrometer. The zirconium filters are each 200 nm thick, however the surfaces of these filters are prone to oxidation. Therefore, we assume a 20 nm thick oxide layer on each surface [26], leading to a total transmission of ~6% [61]. We assume a transmission of 1% for the spectrometer. This gives a harmonic flux of ~$10^6$ photons/sec/harmonic emitted from the source.

We compare our estimated high-energy circularly polarized harmonic flux to that obtained in the collinear geometry by Fan, et al. [26]. They used collinear mixing of circularly polarized counter-rotating 1300 nm and 790-nm driving lasers to produce circularly polarized high harmonics in neon gas in a waveguide geometry. With this scheme they obtain circularly polarized harmonics ranging from ~80–120 eV with a flux of ~$5\times10^7$ photons/sec/harmonic. Therefore, the flux obtained in the noncollinear geometry is about an order of magnitude lower than the flux in the collinear geometry. However, increasing the gas pressure in the interaction region can further increase the noncollinear flux, as it was not yet absorption limited.

## Appendix H: Angular separation of high harmonic orders without a spectrometer

We use noncollinear HHG to demonstrate the separation of the 13th and 15th harmonic orders in the far field without a spectrometer. This is possible because different harmonic orders are emitted at different angles. However, at our driving laser angular separation ($\theta_1$ = 25 mrad) we would not have been able to achieve complete angular separation if the 17th or higher order harmonics were present (Fig. 10).

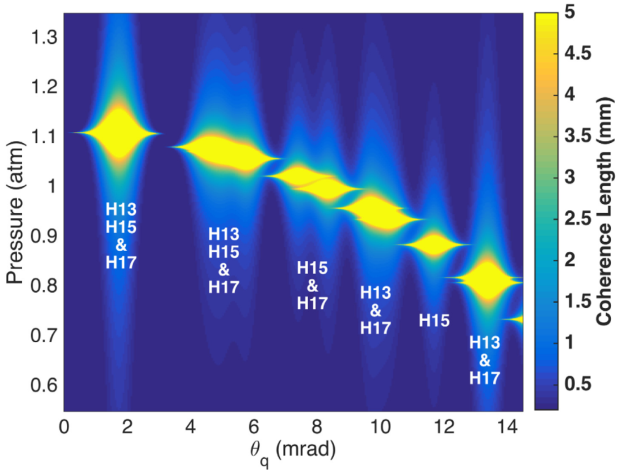

Fig. 10. Coherence length of the 13th, 15th, and 17th harmonic orders from 790 nm driven noncollinear high harmonic generation. While the 13th and 15th harmonic orders can be separated with a modest driving laser angular separation of $\theta_1$ = 25 mrad a larger driving laser angular separation would be required if the 17th harmonic order was present.

## Funding

Department of Energy BES Award DE-FG02-99ER14982. MURI grant from the Air Force Office of Scientific Research under Award Number FA9550-16-1-0121. National Science Foundation Graduate Research Fellowship (DGE-1144083). Junta de Castilla y León (Project SA046U16) and Spanish MINECO (FIS2013-44174-P, FIS2016-75652-P).

### Acknowledgments

M.M. and H.K. acknowledge support from the Department of Energy BES Award DE-FG02-99ER14982 for the experimental work. M.M., H.K. and C.D. acknowledge support from a MURI grant from the Air Force Office of Scientific Research under Award Number FA9550-16-1-0121, and C.H-G. acknowledges support from Junta de Castilla y León (Project SA046U16) and Spanish MINECO (FIS2013-44174-P, FIS2016-75652-P), for the theoretical work. J.E. and C.M. acknowledge support from National Science Foundation Graduate Research Fellowships (DGE-1144083).